

# Magnetoresistance and collective Coulomb blockade in super-lattices of CoFe nanoparticles

R. P. Tan<sup>1</sup>, J. Carrey<sup>1,\*</sup>, C. Desvaux<sup>2</sup>, L.-M. Lacroix<sup>1</sup>,  
P. Renaud<sup>2</sup>, B. Chaudret<sup>3</sup>, M. Respaud<sup>1,\*</sup>

<sup>1</sup> Université de Toulouse; INSA, UPS; LPCNO, 135, av. de Rangueil, F-31077 Toulouse, France  
CNRS; LPCNO, F-31077 Toulouse, France

<sup>2</sup> Semiconductor Products Sector, Freescale, le Mirail B.P. 1029, 31023 Toulouse Cedex, France

<sup>3</sup> Laboratoire de Chimie de Coordination-CNRS, 205 rte de Narbonne, 31077 Toulouse cedex 4, France

## Abstract :

We extensively report on magneto-transport properties of millimetric super-lattices of CoFe nanoparticles surrounded by an organic layer. Superlattices with different nanoparticle sizes and organisations were measured. The resistance-temperature characteristics follow  $R = R_0 \exp[(T_0/T)^{1/2}]$  with  $T_0$  ranging from 13 to 256 K. At low temperature samples with an opened Coulomb gap follow  $I \propto [(V-V_T)/V_T]^\xi$  with  $\xi$  ranging 3.5 to 5.2. Their current-voltage characteristics superpose on a universal curve when shifted by a voltage proportional to the temperature.  $\xi = 1$  is found for a sample with a very large size distribution of nanoparticles. Between 1.8 and 10 K a high-field magnetoresistance with large amplitude and a strong voltage-dependence is observed. Its amplitude only depends on the magnetic field/temperature ratio. Its origin is attributed to the presence of paramagnetic states present at the surface or between the nanoparticles. Below 1.8 K, this high-field MR abruptly disappears and inverse tunnelling magnetoresistance is observed, the amplitude of which does not exceed 1%. At this low temperature, some samples display in their  $I(V)$  characteristics abrupt and hysteretic transitions between the Coulomb blockade regime and the conductive regime. The increase of the current during these transitions can be as high as a factor 30. The electrical noise increases when the sample is near the transition. The application of a magnetic field decreases the voltage at which these transitions occur so magnetic-field induced transitions are also observed. Depending on the applied voltage, the temperature and the amplitude of the magnetic field, the magnetic-field induced transitions are either reversible or irreversible. These abrupt and hysteretic transitions are also observed in resistance-temperature measurements. These collective effects are thought to be due to the strong capacitive coupling between nanoparticles. They could be the soliton avalanches predicted by Sverdlov *et al.* [Phys. Rev. B 64, 041302 (R), 2001] or could also be interpreted as a true phase transition between a Coulomb glass phase or a charge-ordered phase to a liquid phase of electrons.

## PACS :

Coulomb blockade, 73.23.Hk

Spin-polarized transport processes, 72.25.-b

Electrical conductivity of disordered solids, 72.80.Ng

## I. Introduction

Arrays composed of magnetic nanoparticles (NPs) separated by an insulating tunnel barrier have attracted attention because they display both tunnel magnetoresistance (TMR) and Coulomb blockade properties. The tunnel magnetoresistance is due to the fact that the electron tunnel rate between two spin-polarized particles depends on the angle between their magnetization. In the simplest model, assuming that electrons tunnel sequentially between NPs and that the nanoparticles have random magnetizations at the coercive field of the array, the TMR ratio is given by [1]:

$$\text{TMR} = (R_{\text{AP}} - R_{\text{P}}) / R_{\text{P}} = 2P^2 / (1 + P^2), \quad (1)$$

where  $R_{\text{AP}}$  is the resistance at the coercive field of the array,  $R_{\text{P}}$  the resistance when the NPs are magnetically saturated, and  $P$  their spin polarisation. Even with a complete spin polarisation of the NPs ( $P = 1$ ), the maximum TMR value which can be reached in these systems is 100 %. This is due to the fact that an anti-parallel alignment of the NP magnetization is never reached in these arrays, contrary to magnetic tunnel junctions, in which TMR can in principle be infinite using perfectly spin-polarised materials. When the nanoparticles are composed of the standard 3d metals (Fe, Co, Ni) and their alloys, for which the maximum spin polarisation is about 50 % [2], the maximum TMR ratio expected is thus 40 %. We will see below that this maximum value can be higher when the transport between nanoparticles occurs via co-tunnelling. However, when this effect is not present, experimental TMR values reported in arrays of 3d metal nanoparticles never exceed a few tens of percent [3,4,5] as predicted by this basic model.

Coulomb blockade in arrays of NPs has a pure electrostatic origin and is due to the energy  $E_C$  necessary to add a new charge to a NP with a finite capacitance or to move a charge between neighbouring NPs [6,7,8].  $E_C$  depends on the self-capacitance of the NPs and on their mutual capacitive coupling. A well-known consequence of the Coulomb blockade in arrays of NPs is the apparition of a gap in the current-voltage [ $I(V)$ ] characteristics of the arrays below a temperature  $T$  such that  $k_B T \ll E_C$ . Above this gap, numerical studies have shown that the  $I(V)$  characteristics follows at  $T=0$ :

$$I \propto [(V - V_T) / V_T]^\zeta, \quad (2)$$

where  $V_T$  is the threshold voltage above which conduction occurs and  $\zeta$  an exponent related to the dimensionality of the array [6,7,9]. This power-law increase of the current above  $V_T$  is related to the progressive opening of conduction channels in the array. For voltages well above  $V_T$ , the differential conductivity reaches a linear regime [8].  $\zeta = 1$  and  $\zeta = 5/3$  have been calculated for 1D and 2D arrays of disordered nanoparticles respectively. No theoretical value has been calculated for 3D arrays, even if larger values than for the 2D case are expected. Besides, the evolution of the low-bias resistance as a function of the temperature in an array of NPs is expected to follow [10]:

$$R = R_0 \exp\left[(T_0 / T)^\nu\right], \quad (3)$$

where  $R_0$  is the high-temperature resistance,  $T_0$  the activation temperature for charge transport in the array and  $\nu$  an exponent generally found equal to 0.5. The appropriateness of Equ. (2) and (3) to fit experimental data has been shown in many studies on arrays of magnetic and non-magnetic NPs [11, 12, 13].

Arrays of NPs in the Coulomb blockade regime can also present other peculiar properties due to the capacitive coupling between NPs. For instance, a frustrated and non-ergodic phase called "Coulomb glass" is expected to appear in such systems, resulting from the interaction

between electrostatic forces and charge disorder in the array [14]. In this state, slow relaxation, aging and hysteretic phenomena are expected. Collective effects such as avalanches have also been predicted when NPs are strongly coupled [15]. However, these effects have so far not been observed in arrays of nanoparticles but only in granular metals [16,17] and doped semiconductors [18], which are also disordered arrays of localised interacting electrons.

Finally, the interplay between Coulomb blockade and tunnel magnetoresistance leads to various effects, which have been recently reviewed by Yakushiji *et al.* [19]. Notably, in arrays of nanoparticles, when co-tunneling occurs, i.e. when an electron tunnels to a distant NP via other ones, the TMR is enhanced. This enhancement depends on the order of the co-tunneling and has been experimentally observed in insulating Co-Al-O granular films [20]. The TMR was 22 % in the Coulomb blockade regime versus 8 % outside the Coulomb blockade regime.

We recently reported the observation of several novel transport features in three-dimensional super-lattices of CoFe NPs [21,22,23,24]: i) a large high-field magnetoresistance which could reach up to 3000 % ii) the presence of hysteretic step jumps between two states in the  $I(V)$  characteristics of samples in the Coulomb blockade regime iii) in the latter samples, the possibility to induce the transition between the two states by a magnetic field iv) a low field MR with a complex shape. Thus these superlattices display several mechanisms of MR which can obviously not be explained by the standard mechanisms of MR presented above, and also a novel type of coupling between the Coulomb blockade and the magnetic field. In this article we report on the properties of six samples which were extensively measured and analysed. We will stress on the common points and the differences between the samples, so that a global view of their properties can be drawn. Many details and data will be provided, given the complexity and the novelty of these observations (section III). The various results will be discussed in section IV.

## II. Experiments

An organometallic approach consisting on the co-decomposition of two precursors in the presence of stabilizing agents was used to synthesize the FeCo nanoparticles superlattices. The variation of the ligands yielded different materials referred as 1 OA, 1 OA+1 SA, 2 OA in Table I (see below). The principle of the synthesis has been reported in details elsewhere [25]. Briefly, one equivalent of the cobalt precursor  $[\text{Co}(\eta^3\text{-C}_8\text{H}_{13})(\eta^4\text{-C}_8\text{H}_{12})]$  was mixed in toluene under inert atmosphere with 2 equivalents of the iron precursor  $[\text{Fe}(\text{CO})_5]$  in the presence of: i) 1 equivalent of oleic acid (1OA, Sample D); ii) 2 equivalents of oleic acid (2 OA, samples A and E); iii) 1 equivalent of oleic acid and 1 equivalent of stearic acid (1 OA+1 SA, samples B and C). The reaction mixture was then heated to 150°C under 3 bars of dihydrogene. At the end of the synthesis, the super-lattices were collected as small needles and connected using Au wires and silver paint in a glove box under Ar atmosphere. The typical distance between the two contacts is 0.5 mm with around 30000 nanoparticles measured in series/parallel. The time to transfer the connected samples from the glove box to the inside of the cryostat was kept to a minimum (few tens of seconds) to prevent oxidation. Magnetotransport measurements were performed in a Cryogenic cryostat equipped with a superconducting coil using a Keithley 6430 sub-femtoamp source meter. In these experiments, the magnetic field was applied perpendicularly to the current and to the longest axis of the superlattice, with a constant sweep rate in the range of 0.009 T/s.

## III. Results

## A. Structural and magnetic characterisations of the superlattices

A full paper will be soon dedicated to the synthesis of the FeCo nanoparticles and the influence of each parameter on their size, shape, organization and properties. Briefly here, the composition of the obtained material was set to 60 % iron and 40 % cobalt by controlling the metallic precursor ratio in the synthesis (Fe/Co=2/1).

The obtained material consists of nanoparticle superlattices, i.e. compact solids within which the organization of the particles depends on the ligands used. When 1 eq. acid oleic (sample D) or a mixture of 1 eq. oleic acid and 1 eq. stearic acid (samples B and C) is used as stabilizing agents, very monodispersed 15 nm particles are obtained. They spontaneously self-organize in a long range order (as visible on a microtomy cut of a sample [25]) to form supercrystals. When 1eq. oleic acid and 1 eq. stearic acid are used it is even possible to see the fcc packing of the particles in SEM (see Fig. 1b). When 2 eq. of oleic acid are used (sample A), however, the particles are bigger (25 nm diameter) and less monodisperse. This leads to a lack of straightforward arrangement of the particles within the superlattices, which consist of densely packed nanoparticles with no long range spatial ordering.

Magnetization characteristics on a powder composed of many superlattices is shown in Fig. 2(a). The saturation magnetization  $M_S = 163 \text{ A.m}^2.\text{kg}_{\text{FeCo}}^{-1}$  at 2 K is lower than the bulk alloy ( $M_S=240 \text{ A.m}^2.\text{kg}_{\text{FeCo}}^{-1}$ ). PEELS analysis show that the particles display an onion-like structure consisting of a cobalt-rich core surrounded by an iron-rich shell, itself surrounded by another cobalt-rich shell [21]. This segregated structure is partially responsible for the low magnetization. A coercive field of 10 mT and a saturation field of 1.2 T are measured at 2 K. No oxidation is detected, either in WAXS, EELS or in the magnetic measurements. Moreover, the bulk magnetization of FeCo is recovered after annealing which leads to the redistribution of the atomic species and the recrystallization of the particles in the bcc alloyed phase. In Fig. 2(b) magnetization curves measured on a single superlattice are shown. It has been measured successively with the magnetic field perpendicular and parallel to its longest axis. The coercive field is independent of the magnetic field orientation and equals 5 mT but the saturation field is slightly higher in the perpendicular direction (0.9 T) than in the parallel one (0.75 T).

Finally, sample X results from a synthesis involving 1 eq. oleic acid and 1 eq. stearic acid. Still, a problem in the manipulation or with the products purity led to a totally different material. The composition of the material was found to be 30 % iron and 70 % cobalt. The nanoparticles were extremely polydisperse, with typical sizes ranging from 15 to 50 nm. Fig1(d) and 1(e) show a SEM micrograph of the sample X and a TEM micrograph of a superlattice from the same synthesis after dissolution of the nanoparticles in THF. In spite of this polydispersity, the nanoparticles were still compactly packed in millimetre-size superlattices, which made this sample a good candidate to test the influence of structural disorder and of size distribution on the transport properties. As will be more evident below, the transport properties of this sample were indeed of particular interest.

## B. Room temperature resistances and choice of the samples.

All the samples measured displayed at room temperature linear  $I(V)$  characteristics. The room temperature resistances were measured in a range between 8 k $\Omega$  and 5 G $\Omega$ . One possible hypothesis to explain this broad distribution could have been that the contact resistance between the silver grains of the silver painting and the superlattices itself. To test this hypothesis, we have

also measured the room temperature resistances of superlattices on which we had evaporated a layer of gold with a 20  $\mu\text{m}$  gap before connecting them with silver painting. This seems to have no effect on the values of the resistances so the origin of the broad dispersion is probably inherent to the structural properties of the superlattices themselves. We think that either an intrinsic variation in the thickness of the organic tunnel barriers surrounding the NPs or microcracks inside the samples are at the origin of the dispersion. In Table I are summarized the room temperature resistances of the samples which will be presented in this article. It must not be believed that statistical conclusions on the resistance of the superlattices can be deduced from this table. Indeed, as will be detailed below, the low-resistance superlattices were the only ones to display hysteretic jumps in their  $I(V)$  at low temperature. We thus connected inside the glove box many samples, checked their resistances *in situ* and measured extensively only the low-resistance ones. Some samples were also only briefly measured at low temperature, did not show any jump in their  $I(V)$  and were as a consequence not further investigated. They are not included in Table I.

### C. Coulomb blockade properties

All the samples displayed a strong increase of their low-bias resistance when decreasing temperature combined with the apparition of non-linearity in their  $I(V)$  characteristics. As explained in the introduction these are two features typical of Coulomb blockade in arrays of nanoparticles. Fig 3 shows the  $R(T)$  characteristics measured on the samples. Given the large dispersion in their resistances, the voltage bias used to measure them varies from sample to sample and was chosen so the resistance is still measurable at low temperature. This voltage is indicated in parentheses in the “ $T_0$ ” column of Table I. The  $R(T)$  are expected to follow equation (3), with a coefficient  $\nu$  equal to 0.5. This is indeed verified between 100 and 10 K for all the samples (see Fig. 3). Samples D and X display below 10 K a slight deviation to this law with an additional enhancement of the resistance. The activation energy  $T_0$  for charge transport in the array is deduced from the linear slope between 10 and 100 K. Their values range from 13 to 256 K and are summarized in Table I.

Low-temperature  $I(V)$  characteristics of arrays of nanoparticles in the Coulomb blockade regime are expected to follow equation (2). As will be detailed in section D, some samples display below 1.8 K avalanches in their  $I(V)$  which cannot be analysed in this framework. Thus we only analyse in this section the  $I(V)$  characteristics measured at the lowest temperature possible but above the onset of avalanches. These  $I(V)$  are summarized in Fig. 4. To deduce  $\zeta$  and  $V_T$  values from these data, we first plot the function  $I \cdot dV/dI$  versus  $V$ , which is linear above  $V_T$  and allows one to determine  $\zeta$ . These plots are displayed in the insets of Fig. 4. Then the value of  $\zeta$  is used as a fixed parameter in a classical least-square fit of the  $I(V)$  curve, from which the  $V_T$  value is deduced. Samples A and C do not display clear visible gap in their  $I(V)$  characteristics so the  $V_T$  values extracted from these fits are almost null. They also display a rather low  $\zeta$  value compared to the other samples. This is due to the fact that Equ. (2) is in principle strictly valid at  $T=0$ , or at least at a low enough temperature so a clear gap is visible and that the only effect of the temperature is to enlarge the gap without modification of the  $I(V)$  curvature (see below). For samples A and C, this condition is not fulfilled, presumably because the Coulomb gap opens at an even lower temperature. Sample B, D and E display a clear gap in their  $I(V)$  characteristics and physically reasonable values of  $\zeta$  and  $V_T$  are deduced (see Table I). However, it must be pointed out that there is a strong dependency between the  $\zeta$  and  $V_T$  variables in a least square fit. To

illustrate this we also display in Table I fitting results where we arbitrary put  $V_T$  to another value for which the fit is still very good (the chi-square value is increased by a factor two and the two fits cannot be distinguished with the eye). These results show that the error bar on the  $\zeta$  values is around 1. Sample X has a very peculiar and unusual  $I(V)$  characteristic, which has to our knowledge never been reported in large arrays of nanoparticles : just above  $V_T$ , the  $I(V)$  is linear, with a transition between the Coulomb gap and this linear part which is extremely narrow, meaning that all the conduction channels open very rapidly when the voltage is increased above  $V_T$ . In these conditions, it is not possible to deduce  $\zeta$  from the  $I(V)$ , or it can alternatively be said that  $\zeta = 1$  for this sample.

We now analyse the evolution of the  $I(V)$  characteristics as a function of the temperature. In the framework developed by Parthasarathy *et al.* [9], when the Coulomb blockade regime is fully established, it is expected that the  $I(V)$ s measured at various temperatures can collapse on a single curve when shifted by a temperature-dependant voltage. This analysis is presented for samples B and D in Fig. 5. For these samples, the shifted  $I(V)$ s collapse on a single curve in the range 1.7-3.7 K and 1.8-10.5 K, respectively (see Fig. 5(b) and 5(d)). At higher temperature, only the high voltage part of the  $I(V)$  could collapse, but the non-linear part of the  $I(V)$ s at lower voltage do not superpose since the Coulomb gap is not fully established. Fig. 5(e) shows that the voltage used to shift the  $I(V)$ s is linear as a function of temperature. Additionally, it can be noticed the very peculiar behaviour of sample X, clearly different from the other samples and from what is reported in the literature, shown in Fig. 5(f) : the  $I(V)$  characteristics measured at various temperatures on sample X reach the same curve at high voltage, as if the sample was in a purely metallic state at high voltage.

#### D. Collective Coulomb blockade and magnetic-field induced switching

Samples A, C and X display below 1.8 K abrupt jumps in their  $I(V)$ s correlated with the apparition of an hysteretic behaviour. From the samples presented in this article and from other samples measured, it appears that these phenomena are only observed in samples with a low room temperature resistance. The  $I(V)$  characteristics for sample A, C and X are displayed in Fig. 6(a), 6(d) and 7(a), respectively. In all cases, the jumps from the resistive state to the conductive one are correlated with a clear increase of the differential conductivity. The amplitude of these jumps are different on the three samples and are summarized in Table I : their maximum amplitude is 36 %, 120 % and 3000 % for sample A, C and X respectively. In the three samples, the application of a magnetic field has an influence on the transition voltage and on the hysteresis, which is shown in Fig. 6(b), 6(e) and 7(d), but this influence is not similar in the three samples. In sample A, the hysteresis is not well defined, since the current for  $\mu_0 H = 0$  T oscillates telegraphically between the conductive and the resistive state, but with a higher probability to be in the resistive state during the sweep up, and a higher probability to be in the conductive state on the sweep down (see Fig 6(a) and 6(b)). Upon the application of a magnetic field, the hysteresis is shifted toward the left and its area shrinks (see Fig. 6(b)). In sample C, the evolution of the hysteresis was measured as a function of the temperature. At  $T = 1.76$  K, it is poorly defined, similarly to the one observed in sample A. When lowering the temperature, it evolves progressively to a well-defined hysteresis, with an abrupt jump on the sweep up and on the sweep down (see Fig. 6(d)). In this case, the application of the magnetic field slightly shifts the whole hysteresis toward the left (see Fig. 6(e)). In sample X, there is a huge jump in the current in the

sweep up, but no jump in the sweep down (see Fig. 7(a)). In this case, the effect of the magnetic field is to shift the jump on the sweep up toward the left (see Fig. 7(d)). It can be observed that the shift in voltage due to the magnetic field is much larger in this sample than in sample C.

In the three samples, due to the influence of the magnetic field on the hysteresis, it is also possible to directly induce a transition between the two states when a constant voltage is applied (see Fig. 6(c) and 7(e)). The applied voltage must be carefully chosen because the magnetic field has an influence on the  $I(V)$  characteristic on a limited range of voltage. Typically, to induce a transition from the resistive state to the conductive one, the sample must be placed in the resistive state and measured at a voltage slightly below the transition voltage. These transitions can be reversible or irreversible, this (ir)reversibility being directly correlated to the evolution of the  $I(V)$  under the application of the magnetic field. For instance an irreversible transition induced on sample X is shown in Fig. 7(e). The sample is placed in the resistive state at  $V = 36$  V and the magnetic field is increased. For  $\mu_0 H = 2.65$  T, the sample switches to the conductive state. In agreement with this observation, it is seen in Fig. 7(d) that the transition voltage in the  $I(V)$  characteristic crosses  $V=36$  V for a magnetic field between  $\mu_0 H = 2.65$  T and  $\mu_0 H = 4.6$  T. When the magnetic field is swept back to zero, the sample stays in the conductive state. This is again in agreement with Fig. 7(d) which shows that the sample, once in the conductive state at 36 V, is not influenced by the magnetic field. In Fig. 6(c), a reversible transition induced in sample A is shown: the sample is measured at  $V = 50$  V, and the sample switches between the conducting and the resistive state around 1.5 T. The reversibility is in agreement with Fig. 6(b). Indeed, it shows that for  $\mu_0 H = 0$  T, the hysteretic part starts above 50 V, and for  $\mu_0 H = 3$  T, the hysteretic part ends around 50 V. This means that at  $V = 50$  V, only one state is possible for  $\mu_0 H = 0$  T (the resistive one), and one state is possible for  $\mu_0 H = 3$  T (the conductive one) thus excluding hysteretic phenomena at  $V = 50$  V. In sample C, since the shape of the hysteresis evolves from a small area hysteresis at 1.8 K to a large area one at 1.55 K, both types of transitions can be observed: the reversible one at 1.8 K and the irreversible one at 1.55 K. These transitions have been previously published [21] and are not reproduced in this article. It can be noted that this notion of (ir)reversibility depends on the magnetic field and on the applied voltage. For instance, given the evolution of the  $I(V)$  characteristics of sample C with the magnetic field at 1.55 K (see Fig. 6(e)) and assuming that the hysteresis keeps on shifting to the left at higher magnetic field, it is likely that reversible transitions could be observed at  $T = 1.55$  K at the condition to measure the sample at  $V = 16.5$  V and with a maximum magnetic field around 25 T.

We now present the fact that the abrupt and hysteretic transitions between the conductive and the resistive state can also be observed as a function of the temperature. In Fig. 7(b)  $I(V)$  characteristics measured on sample X are shown on a semi-logarithmic scale. It can be seen on this figure that the transition below 1.8 K goes with by an abrupt increase of the transition voltage inducing a "no man's land" area in the upper right quarter of this graph. From this graph, it is expected that this area can be crossed as a function of the temperature at the condition that the applied voltage is above 30 V. Fig. 7(c) displays  $R(T)$  experiments during which the temperature is slowly swept up and down, with a constant voltage applied to the sample. When this voltage is 30 V, the sweeps up and down are superposed, confirming that the experiment is slow enough so that there is no lag between the temperature measured on our sensor and the temperature of the sample. When the voltage is 35 or 40 V, hysteresis and abrupt jumps appear in the  $R(T)$ , with a hysteresis width around 300 mK, as expected from Fig. 7(b).

#### E. Magnetoresistance for $T > 1.8$ K

All the samples display a large high-field magnetoresistance in the range 1.8-15 K. The maximum amplitude measured varies from sample to sample and is summarized in the column "high-field MR" of Table I. The highest magnetoresistance value was observed in sample B and reached 3000 % [22]. All the samples present a similar evolution of the magnetoresistance amplitude as a function of the temperature, which is summarized in Fig. 8(a) for samples B, C and D: the MR ratio increases when the temperature is lowered until an abrupt drop of its amplitude occurs below 1.8 K. We present now detailed results on the magnetoresistance properties above 1.8 K of sample D, which are representative of all the sample properties. Detailed results on samples B and C in this regime can be found elsewhere [21,22]. In Fig. 8(b), a typical  $R(H)$  measured on sample D is shown. The  $R(H)$  characteristics have always a butterfly shape and do not saturate at high magnetic field, even when a 9 T magnetic field is applied [22]. The butterfly shape is due to the fact that there is a lag of around 90 s between the variation of the magnetic field and the associated variation of resistance in the sample. To illustrate this point, we show in Fig. 8(c) an experiment during which the resistance of the sample is measured as a function of time when the magnetic field is swept from 0 to 2.6 T and then back. The times at which the magnetic field starts and stops its variation are indicated as vertical lines. During the sweep up, the resistance starts varying around 90 s after the start of the sweep. Similarly, the resistance stabilizes to its final value around 90 s after the magnetic field has stabilized. In Fig. 8(d), magnetoresistance curves measured at various temperatures ranging from 2.08 K to 13.5 K are plotted as a function of the ratio  $H/T$ . They superpose on a universal characteristic, from which it is deduced that the MR amplitude only depends on the  $H/T$  ratio.

In Fig. 8(e), the voltage dependence of this high-field MR is shown. Three different methods of measuring this voltage dependence are compared. Blue dots display MR ratios deduced from individual  $R(H)$  characteristics measured at various voltages. Black line and red open dots corresponds to the MR values deduced from two  $I(V)$  characteristics measured at zero field and 2.6 T. Black line originates from  $I(V)$  characteristics measured using a constant current range, which explains the noise at low voltage due to an imprecision in the measurements of low currents. For red dots, the current at various voltages has been manually measured using the best measurement range for each point. As expected, the two last methods give identical results at high voltage. However the MR values deduced from  $R(H)$  measurements are always 20 to 25 % lower than the values deduced from  $I(V)$  characteristics. This is well explained by the dynamical experiments shown in Fig. 8(c) : during  $R(H)$  measurements, the maximum MR value is not reached, since the magnetic field is swept back before the resistance has reached its final stabilized value. From Fig. 8(c), it is deduced that the difference between the dynamical MR and the static MR should be in the range 20-23 %, in good agreement with what is indeed observed in Fig. 8(e).

#### F. Magnetoresistance for $T < 1.8$ K

Below 1.8 K, the high-field magnetoresistance collapses in all the samples. At low temperature, some of them display in a restricted range of applied voltage the magnetic-field induced switching between two states detailed in section D. However, all the samples also display a small amplitude magnetoresistance visible in a large range of applied voltage, which is now detailed. In Fig. 9 the low temperature magnetoresistance properties of sample B are shown. In Fig 9(a) the  $R(H)$  characteristic measured up to 8.8 T evidences the fact that a small-amplitude high-field MR is still present in the samples. However, its characteristics are radically different from the one observed above 1.8 K : it does not display an hysteresis, its curvature is rather

downward than upward and its amplitude is much smaller. The voltage dependence of this high-field MR has not been studied. In Fig. 9(b), 9(c) and 9(d),  $R(H)$  characteristics measured at different voltages and up to 2.7 T are shown. These  $R(H)$  have a shape typical of inverse tunnel MR with two peaks at  $\mu_0 H = \pm 0.1$  T and a saturation around 1 T. The tunnel MR ratio is thus defined using the resistance at the peak and the resistance at the saturation. It evolves from -1.8 % at 90 V to -0.3 % at 200 V on this sample. Superimposed on this tunnel MR, a positive MR peak centred around zero is observed on all the samples. Its amplitude ranges between 0.05 % to 0.1 % in the various samples, and is independent of the applied voltage. When the sample is let relaxing at zero magnetic field during one or two minutes before a MR measurement, this central peak appears more evidently, displaying an enhanced amplitude during the first sweep of the magnetic field. Indeed, during this relaxation, the resistance of the sample slowly increases, reaching a level of resistance which is then never reached again during the MR measurement. This enhanced peak at the first sweep is visible in Fig 9(b), 9(c) and 9(d) for sample B. It is not always trivial to distinguish this peak from the inverse tunnel MR characteristic presented before. In sample C, this distinction is easier and is presented now. In Fig. 10, MR properties of sample C at 1.5 K are shown. In Fig. 10(a), the  $I(V)$  characteristic of this sample at 1.5 K is recalled with vertical lines indicating the various voltages at which subsequent MR measurements have been performed. For an applied voltage of 0.1 V, the inverse tunnel MR and the central peak are both visible, with a MR ratio of -0.8 % for the inverse tunnel MR (see Fig. 10 (b)). For  $V = 16$  V, this MR reduces to -0.16 % and for  $V = 20$  V no inverse tunnel MR is observed; only the central peak is visible (see Figs. 10 (c), 10 (d) and 10 (g)). At 1.5 K, this sample displays in its  $I(V)$  the abrupt transitions described in section D, making possible the measurement of the low-field MR properties for an identical applied voltage  $V = 18$  V but in the two different conduction states. The two measurements are shown in Fig. 10(e) and 10(f), and are labelled as "low state" and "high state" for the resistive and the conductive state, respectively. The inverse tunnel MR completely disappears when the sample changes from the resistive to the conductive state.

#### IV. Discussion

The magnetotransport properties presented in this article are very complex : two novel mechanisms of magnetoresistance with an unusual behaviour were reported. We do not have so far indisputable theories to explain them but only plausible hypotheses. Thus we do not exclude that explanations radically different from the ones we will present could emerge.

We first discuss the classical Coulomb blockade properties presented in section C. It should be first recall that there is so far no experimental studies of Coulomb blockade properties on 3D superlattices of nanoparticles. However  $\xi$  value greater than the one measured in 2D arrays of NPs are expected.  $\xi$  values ranging from 2.01 to 2.27 were reported in arrays in which a single layer of NPs is deposited on a substrate, which is the 2D case [9,11]. Thick arrays of nanoparticles deposited on substrates show an increased values of  $\xi$  ranging from 2.2 to 3 and can be considered as intermediate between the 2D and the 3D case [12,13]. In our samples, as explained in section D, only the  $\xi$  values extracted from samples B, D and E are valuable. They range from 3.5 to 5.2, i.e. much higher than what is reported in the 2D or 2D/3D cases. This confirms the high dimensionality of the current paths in the samples. Numerical simulations of 3D arrays of nanoparticles are still missing to obtain theoretical values of  $\xi$  in the true 3D case.

The presence of hysteretic and abrupt transitions in the  $I(V)$  or in the  $R(T)$  characteristics of the samples, described in section D, has never been reported in arrays of chemically-prepared

nanoparticles. However, related behaviour has been reported in thin films of quenched condensed Al [16] and granular films of Cr [17]. One can also note the similarity between these phenomena and the electric-field induced switching of charge ordered-states observed in manganites [26,27,28,29]. In our system, the abrupt increase of the current and of the differential resistance means that several conduction channels open at the same time in the sample which explains our appellation of "collective Coulomb blockade" for the observed phenomena. Numerical simulations of transport in arrays of nanoparticles have shown or mentioned that hysteresis [6], avalanches [15] or blocking in a metastable state [7] may occur in such systems at the condition that the capacitive coupling between neighbouring nanoparticles  $C$  is much larger than the self-capacitance  $C_0$  of the nanoparticle. This could be the reason for our observation of these phenomena, since our system is composed of NPs which are much larger -and so with a reduced  $C_0$ - than the ones which have been measured in previous studies on arrays of NPs. In large arrays of strongly coupled NPs it has also been predicted that a strong increase of the electrical noise around the transition voltage or even infinite electronic avalanches could occur. We indeed observed an increase of the electrical noise in sample A and C near the transition (see Fig. 6(c) and Ref. [21]) and the abrupt transition from the insulating regime to the conductive one could be interpreted as the creation of an infinite avalanche in the sample. Thus our experimental results could be understood in the framework developed by Sverdlov *et al.* [15] but more precise noise measurements as a function of the temperature and of the applied voltage should be performed to study the link between these numerical studies and our experimental results. Another way of interpreting these experimental results can also be put forward. As mentioned in the introduction, arrays of localised electrons may present at low temperature a frustrated phase called Coulomb glass, distinct from the liquid phase present at higher temperature. In the case of weak disorder, this low-temperature phase can also be a charge-ordered state [14]. Transport properties of these solid phases have never been theoretically studied. However, the features we observed experimentally resemble a true phase transition and could be interpreted as a phase transition between a solid state and liquid state of charges in the super-lattice. The magnetic-field induced transitions indicate that the magnetic field can similarly to the applied voltage bring the energy to the system to trigger the transition. The mechanism for this energy transfer to the magnetic material could be the same as the one responsible for the magneto-Coulomb oscillations in magnetic single-electron transistors [30,31], namely a shift of the Fermi level of the magnetic NPs with the application of a magnetic field due to the Zeeman splitting and to the asymmetry in the density of state at the Fermi level.

We now discuss the high-field MR observed in the samples above 1.8 K and presented in section E. Given its huge amplitude, this high-field MR cannot be attributed to the tunnel MR generally observed in arrays of nanoparticles. Instead it can be observed that this high-field MR displays two features typical of the so-called "colossal magnetoresistance" observed in some magnetic oxides : i) the magnetoresistance is maximum in a high-temperature state before a collapse below a critical temperature ii) the amplitude can easily reach very high values and does not saturate at high magnetic field. Colossal MR is due to the fact that the transfer probability of electrons between two localised paramagnetic sites strongly depends on the angle between their magnetic moments. We interpret the high-field MR in our samples as resulting from the presence of paramagnetic states localised at the surface or between the nanoparticles. This hypothesis is enforced by the  $H/T$  dependence of the MR ratio. These paramagnetic states could result from the coordination of the ligands at the surface of the NPs or to traces of organometallic precursors [22]. We developed a phenomenological model based on this interpretation, which is indeed able to explain the large amplitude of the MR ratio and its strong voltage dependence [23]. However,

further work is needed to prove experimentally our hypothesis. In this framework the abrupt drop of the high-field MR below 1.8 K would be due to a magnetic transition of these impurities to an ordered state.

Below 1.8 K, the observation of an inverse tunnel MR characteristic is coherent with this interpretation of an high-field MR due to impurities. Indeed, inverse tunnel MR is commonly attributed to the transfer between two magnetic electrodes through an impurity inside the tunnel barrier [32,33]. The weak amplitude of the inverse tunnel MR measured in the samples may have two origins. First, the process of tunnelling through an impurity always lead to a strong decrease of the TMR ratio compared to the one with a direct tunnelling. Second, as seen in Fig. 2(b), the remanent magnetization in these superlattices is almost null, which is the sign that the dipolar coupling between the nanoparticles is strong compared to their anisotropy. As a consequence, it is likely that, in the superlattices, the reversal of the magnetization occurs via the collective reversal of large domains composed of ferromagnetically coupled NPs. In this case, the mean angle between adjacent NPs is quite small during the reversal, leading to a reduced TMR compared to a case of a reversal of NPs with strong anisotropies, which is assumed to demonstrate Equ. (1).

A puzzling point of our experimental results is the fact that the disappearance of the high-field MR and the apparition of hysteresis in the  $I(V)$  characteristics both happen below the same critical temperature. In the hypothesis presented above, there should be no link between them since we interpreted the disappearance of the high-field MR as the consequence of a magnetic transition of impurities and the appearance of hysteresis as of pure electrostatic origin. However, it is possible that the magnetic transition could be accompanied by an increase of the capacitive coupling between the nanoparticles thus favouring the apparition of collective effects. Indeed, we have explained the high-field MR by the fact that the parallel alignment of the impurity by the magnetic field leads to an increase of the electronic transmission between nanoparticles. Microscopically speaking, this can be viewed as an increase of the radius of the wave function associated with electrons localised on the nanoparticles. It is conceivable that the transition of the impurity to a ferromagnetic state could be accompanied by an abrupt increase of the radius of this wave function, thus reducing the effective distance between nanoparticles and increasing their capacitive coupling.

Finally, the experimental results obtained on sample X were of great interest since this sample was composed of non-organized broadly-dispersed NPs, but presented the most impressive electrical properties: i) The  $\xi = 1$  value at 1.9 K means that all the conduction channels opened at the same time when it goes out of the Coulomb blockade regime (see Fig. 4(f)). ii) At high voltage, he behaves as a purely metallic sample (see Fig. 5(f)) iii) Below 1.8 K this sample displayed the highest jumps in the  $I(V)$  characteristics and the largest influence of the magnetic field on the threshold voltage (see Fig. 7(d)). This clearly shows that a perfect organization of the NPs inside the super-lattices is not a requirement to observe the collective effects described in this article. We think that the  $C/C_0$  ratio is a more important parameter, as it was already theoretically expected [6,7,15].

## V. Summary and outlook

This article reports on the observation in superlattices of CoFe nanoparticles of two novel mechanisms of MR, both of them leading to huge amplitudes of MR. Further investigations on other systems are needed to prove the origin of these two mechanisms. The high-field MR observed above 1.8 K is thought to be due to paramagnetic states so a way to understand their

nature and to control their presence and density will be pursued. For instance, the volunteer incorporation of organometallic precursors between the nanoparticles will be tried as well as a change in the nature of the ligands surrounding the NPs. The collective effects are thought to have a pure electrostatic origin so they could probably be observed in super-lattices of non-magnetic NPs such as gold. We think that the measurements of large NPs separated by thin tunnel barriers could favour the observation of these phenomena. On one other hand, the magnetic-field induced switching is probably only possible using magnetic NPs, but this should be confirmed experimentally. Finally, enlightening theoretical papers have been devoted to the transport properties of arrays of NPs in the strong coupling limit [7,15] but specific studies on the irreversibility in  $I(V)$  characteristics and on the eventual consequences of a real phase transition on electrical properties are still missing in these systems.

## Acknowledgements :

We acknowledge C. Crouzet and J. Moreau for their building of the sample holder.

## References :

\* Correspondence should be addressed to M. R. and J. C. (marc.respaud@insa-toulouse.fr and julian.carrey@insa-toulouse.fr)

- 
- [1] J. Inoue and S. Maekawa, Phys. Rev. B **53**, R11927 (1996)
  - [2] J. Joshua Yang, C. Ji, Y. A. Chang, X. Ke and M. S. Rzchowski, Appl. Phys. Lett. **89**, 202502 (2006)
  - [3] B. Hackenbroich, H. Zare-Kolsaraki, and H. Micklitz, Appl. Phys. Lett. **81**, 514 (2002)
  - [4] O. Chayka, L. Kraus, P. Lobotka, V. Sechovsky, T. Kocourek, and M. Jelinek, J. Mag. Mag. Mat. **300**, 293 (2006)
  - [5] H. Zare-Kolsaraki and H. Micklitz, Phys. Rev. B **67**, 094433 (2003)
  - [6] A. A. Middleton and N. S. Wingreen, Phys. Rev. Lett. **71**, 3198 (1993)
  - [7] D. M. Kaplan, V. A. Sverdlov, and K. K. Likharev, Phys. Rev. B **68**, 045321 (2003)
  - [8] C. Reichhardt and C. J. O. Reichhardt, Phys. Rev. Lett. **90**, 046802 (2003)
  - [9] R. Parthasarathy, X.-M. Lin, K. Elteto, T. F. Rosenbaum and H. M. Jaeger, Phys. Rev. Lett. **92**, 076801 (2004)
  - [10] K.-H. Müller *et al.*, Phys. Rev. B **66**, 075417 (2002)
  - [11] C. Kurdak, A. J. Rimberg, T. R. Ho, J. Clarke, Phys. Rev. B **57**, R6842 (1998)
  - [12] H. Fan *et al.* Science **304**, 567 (2004)
  - [13] P. Beecher, A. J. Quinn, E. V. Shevchenko, H. Weller and G. Redmond, Nanoletters **4**, 1289 (2004)
  - [14] S. Pankov and V. Dobrosavljević, Phys. Rev. Lett. **94**, 046402 (2005)
  - [15] V. A. Sverdlov, D. M. Kaplan, A. N. Korotkov, K. K. Likharev, Phys. Rev. B **64**, 041302(R) (2001)
  - [16] E. Bielejec and W. Wu, Phys. Rev. Lett. **87**, 256601 (2001)
  - [17] V. A. Krupenin, V. O. Zalunin and A. B. Zorin, Microelectron. Eng. **81**, 217 (2005)
  - [18] E. Leannon and M. Müller, Phys. Rev. B **72**, 174202 (2005)
  - [19] K. Yakushiji, S. Mitani, F. Ernult, K. Takanashi and H. Fujimori, Physics Report **451**, 1 (2007)
  - [20] S. Mitani *et al.*, Phys. Rev. Lett. **81**, 2799 (1998)
  - [21] R. Tan *et al.*, Phys. Rev. Lett. **99**, 176805 (2007)
  - [22] R. Tan *et al.*, J. Magn. Magn. Mater. **320**, L55 (2008)
  - [23] R. Tan, J. Carrey and M. Respaud, J. Appl. Phys., in press
  - [24] R. Tan *et al.*, J. Appl. Phys **103**, 07F317 (2008)
  - [25] C. Desvaux *et al.*, Nature Materials **4**, 750 (2005)
  - [26] A. Asamitsu, Y. Tomioka, H. Kuwahara and Y. Tokura, Nature **388**, 50 (1997)
  - [27] K. Hatsuda, T. Kimura and Y. Tokura, Appl. Phys. Lett. **83**, 3329 (2003)
  - [28] Y. Tokura and Y. Tomioka, J. Magn. Magn. Mater. **200**, 1(1999)
  - [29] H. Kuwahara, Y. Tomioka, A. Asmitsu, Y. Moritomo and Y. Tokura, Science **270**, 961 (1995)
  - [30] K. Ono, H. Shimada and Y. Ootuka, J. Phys. Soc. Jap. **67**, 2852 (1998)
  - [31] H. Shimada, K. Ono and Y. Ootuka, J. Phys. Soc. Jap. **67**, 1359 (1998)

---

[32] E. Y. Tsymbal, A. Sokolov, I. F. Sabirianov and B. Doudin, Phys. Rev. Lett. **90**, 186602 (2003)

[33] J. R. Petta, S. K. Slater, and D. C. Ralph, Phys. Rev. Lett. **93**, 136601 (2004)

**Table**

Sample	Ligands	$R$ (300 K)	$T_0$	$\xi$	$V_T$	high-field MR	avalanches
A	2 OA	400 k $\Omega$	24 K (2 V)	2.5 (b)	0 (b)	not measured	yes (36%)
B [22]	1 OA + 1 SA	5 G $\Omega$	80 K (25 V)	3.5 (fixed) 4.37	33 0(fixed)	3000 %	no
C [21]	1 OA + 1 SA	4.5 k $\Omega$	24 K (10 mV)	1.3 (b)	2 (b)	100 %	yes (120%)
D	1 OA	100 M $\Omega$	256 K (10 V)	5.2(fixed) 4.4	3.2 30(fixed)	90 %	no
E	2 OA	1.2 G $\Omega$	13 K (10 V)	4.9 (fixed) 4.03	24 50(fixed)	160 %	no
X	1 OA + 1 SA (c)	300 k $\Omega$	200 K (20 mV)	1 (a)	30	280 %	yes (3000%)

Table I :

Summary of the superlattice properties. For sample B and C, references of articles in which some of their properties have been previously published is indicated in the first column. The column "ligands" corresponds to the amount and nature of acids and amines used for the synthesis. The subsequent columns display the values of the resistance at room temperature  $R$  (300 K), the activation energy  $T_0$ , the exponent  $\xi$  and the threshold voltage  $V_T$ . In the column " $T_0$ ", the voltage at which the  $R(T)$  has been measured is indicated in parentheses. The column "high-field MR" indicates the maximum high-field MR measured on the sample. The last column indicates if avalanches have been observed in the  $I(V)$  characteristics at low temperature, and provides in parentheses the amplitude of the avalanches. (a) On sample X, the  $I(V)$  characteristics is linear as soon as the voltage is above  $V_T$  (see text and Fig. 4(f)). (b) On these samples, the gap in the  $I(V)$  characteristic at 1.8 K is not clearly defined (c) For sample X, there was a problem during the synthesis (see test).

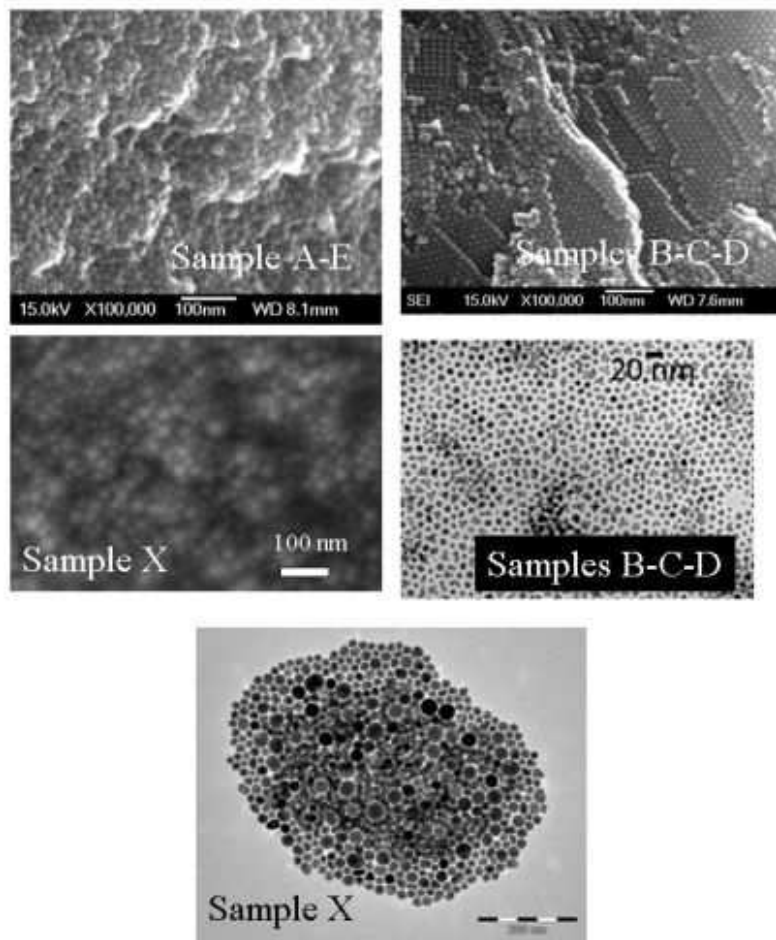


Fig. 1

Fig. 1 : a) b) c) SEM micrographs of superlattices synthesized in various conditions (see table I). The micrographs illustrate the particles size and organisation for a) sample A; b) sample B, C and D; c) Sample X. d) e) TEM micrographs of the nanoparticles after redispersion of the superlattices in solvent for d) sample B, C, and D; e) sample X.

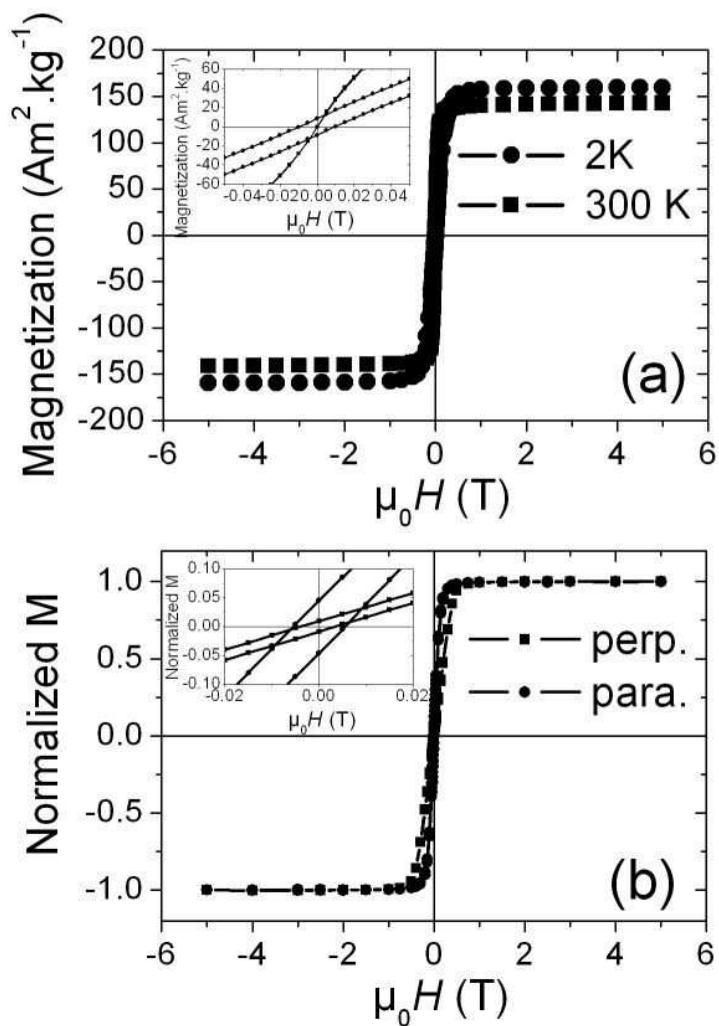
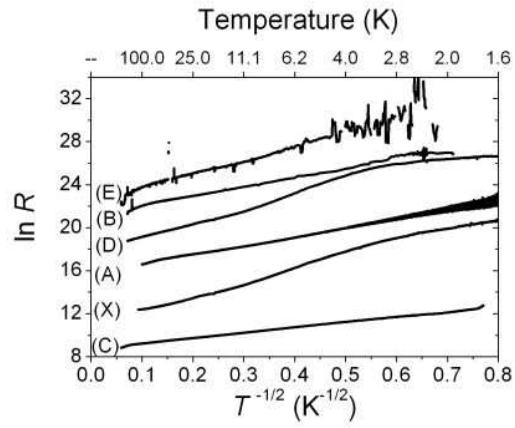


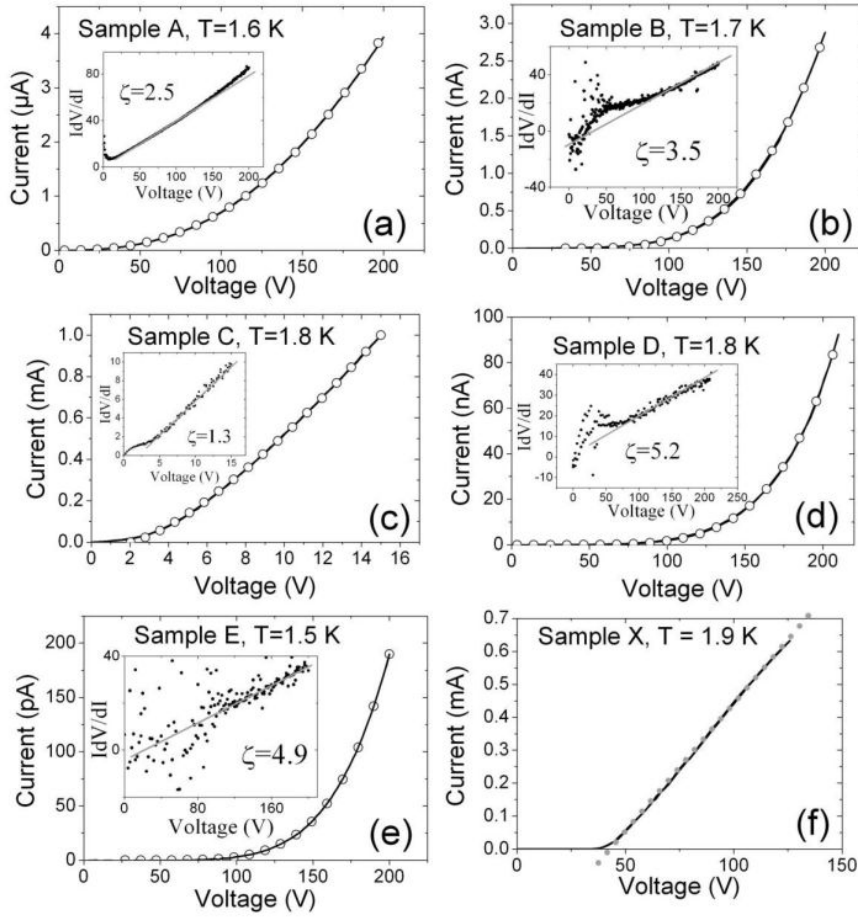
Fig. 2

Fig. 2 : a)  $M(H)$  measured at 2 K and 300 K on a powder composed of a large number superlattices. b)  $M(H)$  of a single superlattice measured with the field perpendicular or parallel to the longest axis of the super-lattice. (insets) Enlarged view of the  $M(H)$ s at low magnetic field.



**Fig. 3**

Fig. 3 : Resistance of the different samples as a function of temperature. The logarithm of the resistance is plotted versus  $T^{-1/2}$ .



**Fig. 4**

Fig. 4 : a) b) c) d) e)  $I(V)$  characteristics of the superlattices (plain lines) and corresponding fits of the characteristics using Equ. (2) (open circles). The measurement temperatures are the ones indicated on the figures. The  $\zeta$  values used for the fits are the ones deduced from a plot of  $I dV/dI$  versus  $V$ , shown in the inset. The  $V_T$  values deduced from the best fits of the experimental data are detailed in Table I. f)  $I(V)$  characteristic at 1.9 K of sample X (plain line). A linear slope is shown as a guide to the eye (dotted line).

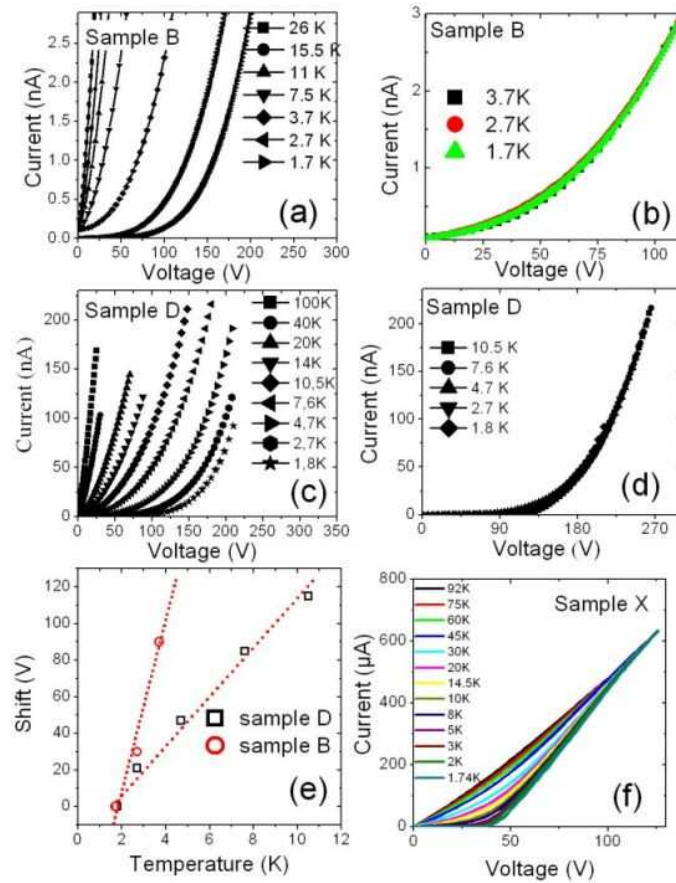
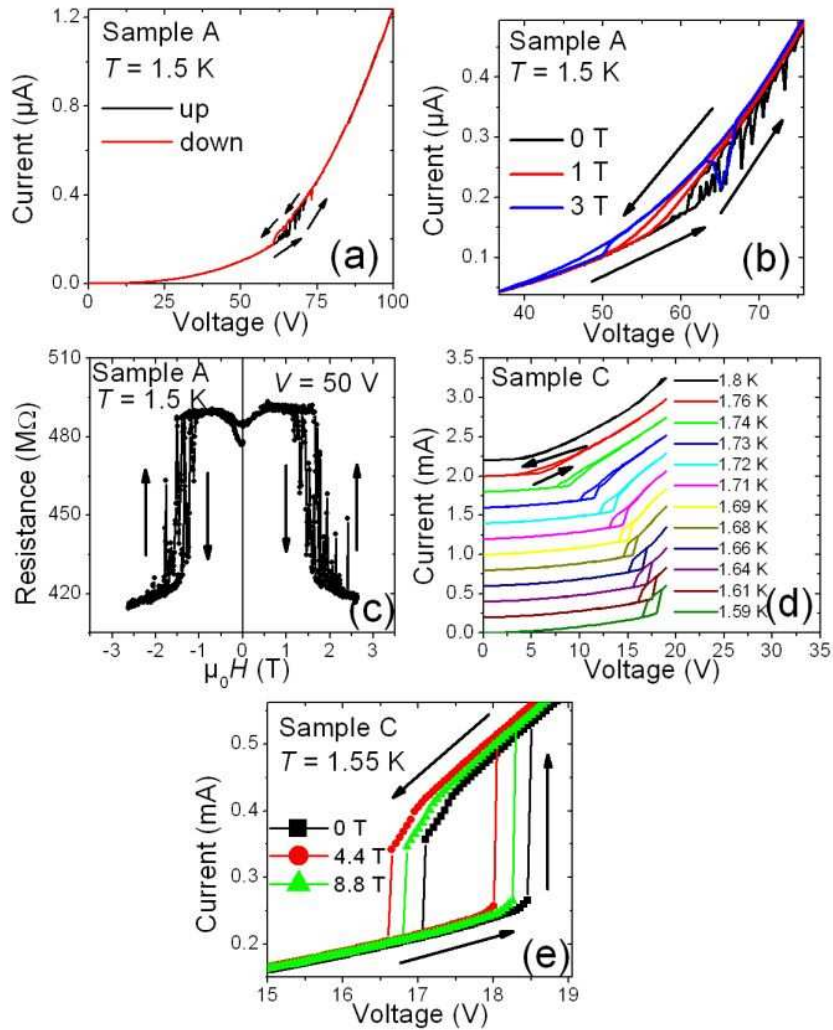


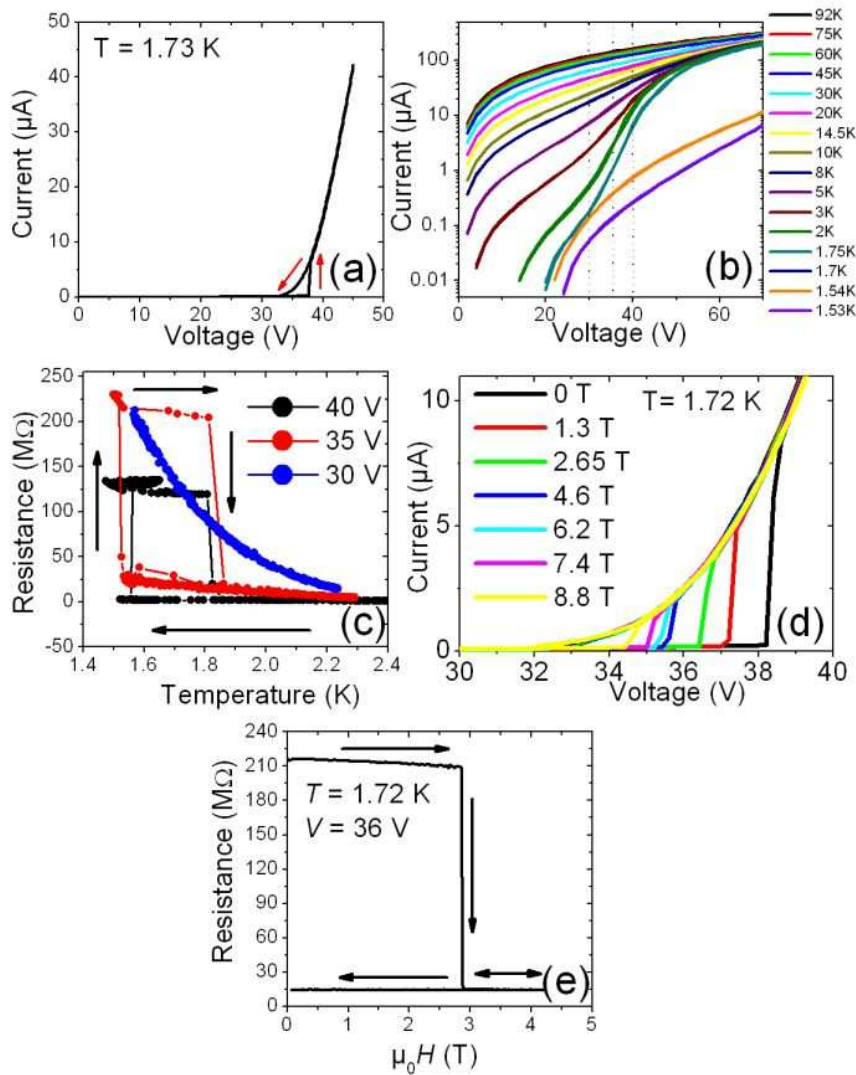
Fig. 5

Fig. 5 : a) c) Evolution of the  $I(V)$ s for samples B and D as a function of temperature. b) d) The  $I(V)$ s at different temperatures for samples B and D are shifted to superpose. e) Summary of the shift values as a function of temperature. Dotted lines are a guide to the eye. f) Evolution of the  $I(V)$ s as a function of the temperature for sample X.



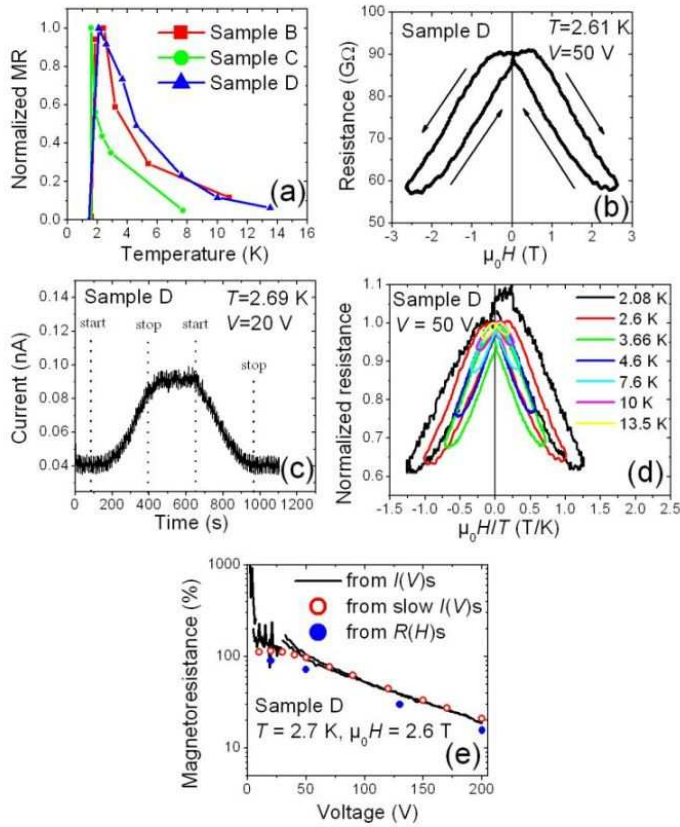
**Fig. 6:**

Fig. 6: a)  $I(V)$  of sample A at 1.5 K. The arrows indicate the voltage sweep direction. b) Evolution of the  $I(V)$  of sample A at 1.5 K under the application of a magnetic field of 0, 1 and 3 T. c)  $R(H)$  of sample A at 1.5 K with a voltage bias of 50 V. The arrows indicate the magnetic field sweep direction. d) Evolution of the  $I(V)$  of sample C as a function of temperature. e) Evolution of the  $I(V)$  of sample C at 1.55 K under the application of a magnetic field of 0, 4.4 and 8.8 T.



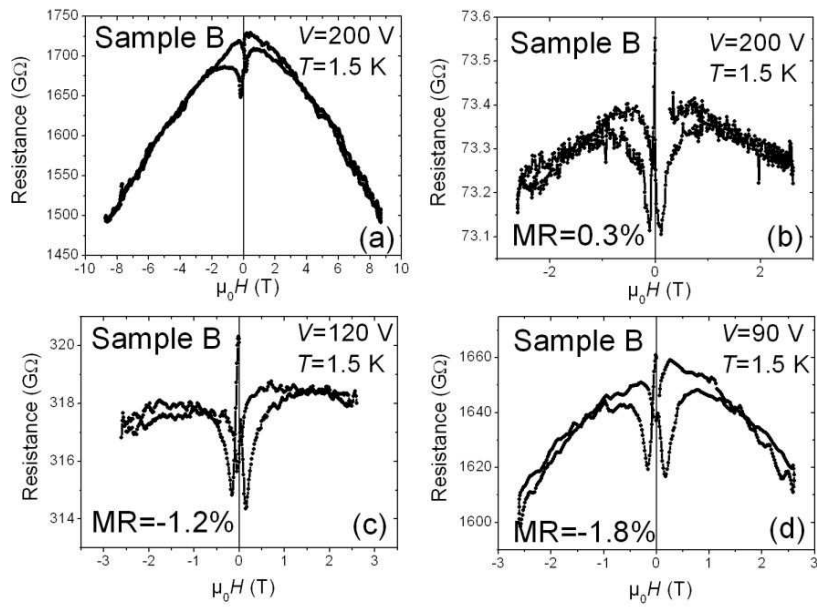
**Fig. 7:**

Fig. 7: Transport properties of sample X. a)  $I(V)$  at  $T=1.73 \text{ K}$ . b)  $I(V)$ s at different temperatures on a semi-logarithmic scale. c)  $R(T)$  measured at 30 V, 35 V and 40 V. The arrows indicate the sweep directions. For the measurement at 30 V, the  $R(T)$  does not display any hysteresis. d)  $I(V)$  characteristics at 1.72 K and different values of the magnetic field. The sweep direction is similar to (a). e)  $R(H)$  measurement at  $T=1.72 \text{ K}$  and  $V = 36 \text{ V}$ . The arrows indicate the sweep direction.



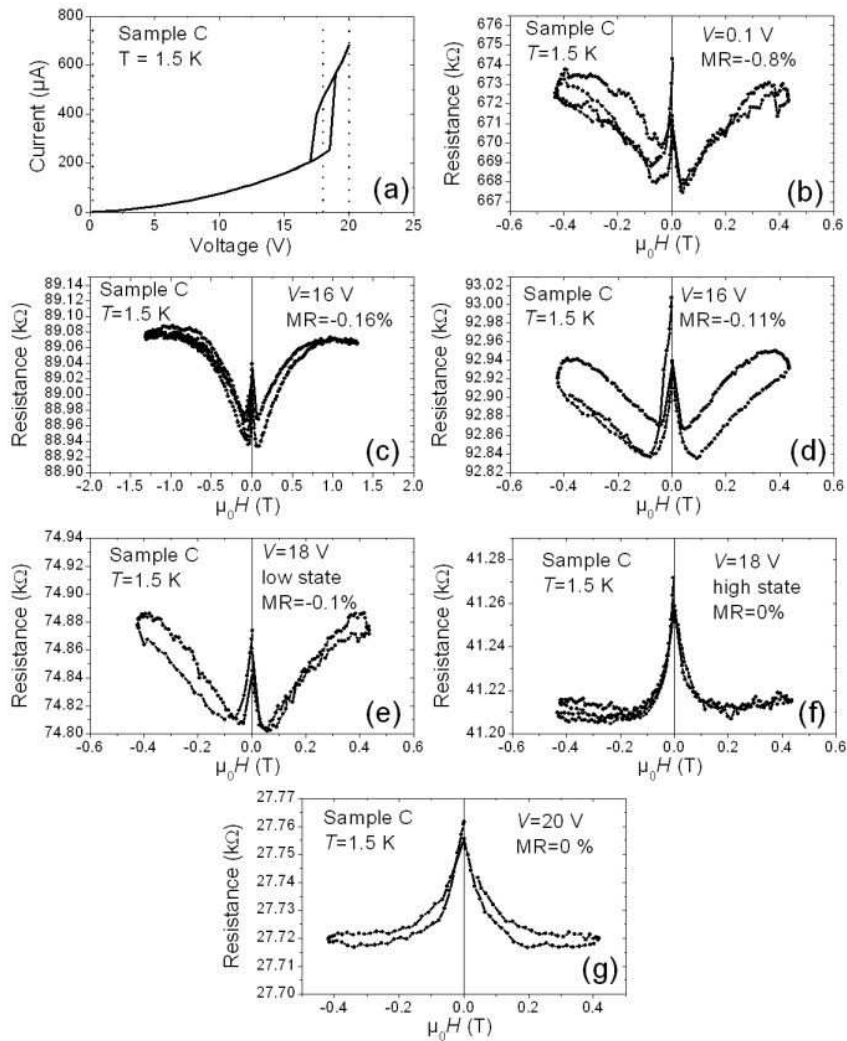
**Fig. 8**

Fig. 8 : a) MR( $T$ ) for samples B, C and D. The MR amplitudes were deduced from  $R(H)$  measurements at 2.6 T and were normalized to the highest value (17 %, 80 % and 64 %, respectively). The applied voltage was 200 V, 20 mV and 50 V, respectively. b)  $R(H)$  on sample D measured at  $T = 2.61$  K and  $V = 50$  V. c) Evolution as a function of time of the current in sample D when the magnetic field is swept from 0 to 2.6 T and then back. The "start" ("stop") corresponds to the start (end) of the magnetic field variation. d)  $R(H/T)$  characteristics for sample D measured at various temperatures with  $V = 50$  V. The resistance has been normalized to its value at zero magnetic field. e) MR( $V$ ) at  $\mu_0 H = 2.6$  T for sample D at 2.7 K. Blue dots corresponds to values deduced from  $R(H)$  measurements at different voltages. Black line and red open dots corresponds to the values deduced from two  $I(V)$  characteristics at zero field and 2.6 T.  $I(V)$  corresponding to the open red dots have been manually measured using the best measurement range for each point.



**Fig. 9**

Fig. 9 : MR of sample B at 1.5 K. The MR value indicated on the figures is taken between the inverse peaks and the plateau at 1 T. a) and b) The voltage bias  $V=200$  V. c)  $V=120$  V. d)  $V=90$  V.



**Fig. 10**

Fig. 10 : a)  $I(V)$  of sample C at 1.5 K. The dotted line indicated the voltages at which the MR measurements have been performed. b) c) d) e) f) g) MR measurements performed on sample C at 1.5 K. The bias voltage at which the MR have been performed are indicated on the figures. For a bias voltage of 18 V, there are two possible states of conduction. For e) the sample is in the resistive state; for f) it is in the conductive state. The MR amplitude indicated on the graphs does not take into account the central peak.